Theoretical Insights into the Stability of Perovskite Clusters by Studying Magnetization and Magnetocaloric Effect of $Nd_{0.6}Sr_{0.4}MnO_3$ Compound at Room Temperature

F. Issaoui[1] · E. Dhahri[2] · E. K. Hlil[3]

Abstract

The $Nd_{0.6}Sr_{0.4}MnO_3$ sample has been synthesized by the solid-state reaction. In this research paper, structural, morphological, magnetic and magnetocaloric properties are reported. The refinement by Fullprof has revealed the coexistence of both Pnma orthorhombic and R-3c rhombohedral phases. The obtained magnetic results show a paramagnetic–ferromagnetic transition at $T_C = 245$ K. The magnetocaloric effect was estimated from the magnetic isotherms. We can estimate that the magnetic entropy change (ΔS) values by the Hamad theory are very close to those obtained using the classical Maxwell relation. Under an applied field 5 T, the maximum of the magnetic entropy change (ΔS) max and the relative cooling power is found to be 3.68 J/kg K and 216.03 J/kg, respectively. The obtained values are compared with those of some other reported manganite and show that our compound could be a promising candidate for magnetic refrigeration. Finally, the construction of the universal curve of the magnetic entropy change confirmed the studied manganite undergoes a second-order magnetic phase transition.

Keywords Phenomenological model · Magnetocaloric effect · Universal curve

1 Introduction

The half-doped manganites $R_{0.5}Sr_{0.5}MnO_3$ (R = Pr, Nd, La) are specially interesting due to their colossal magnetoresistance (CMR) together with their particular phase diagram with respect to other doping concentrations. From room

✉ F. Issaoui
  issawi_fatma@yahoo.fr

1 Research Unit of Valuation and Optimization of Resource, Faculty of Science and Technology of Sidi Bouzid, University of Kairouan, Sidi Bouzid, Tunisia

2 Laboratory of Applied Physics, Faculty of Sciences of Sfax, University of Sfax, Sfax, Tunisia

3 Institut Néel, CNRS et Université Joseph Fourier Grenoble, Grenoble, France

temperature (where they are both in a paramagnetic insulator state) downward, a ferromagnetic metallic phase (FM) is developed at about 250 K, while at lower temperature, they both become antiferromagnetic insulators (AFM) [1, 2]. If CMR were simply described by the double-exchange mechanism (DE), it would be expected that the system in the pure ferromagnetic metallic state had no orbital ordering and showed an isotropic behavior. But the study of the spin dynamics of these materials by neutron scattering measurements has shown the existence of the static d_{x2-y2}-type orbital ordering in both the paramagnetic and ferromagnetic states [3], implying that there is an anisotropic behavior which has been confirmed in the spin wave dispersion in the FM state. Besides, the antiferromagnetic ordering, it is the CE-type AFM spin structure accompanied with charge ordering for $Nd_{0.5}Sr_{0.5}MnO_3$ [4, 5].

The phase diagram is even a little more complex for the case of $Nd_{0.5}Sr_{0.5}MnO_3$ as it has been demonstrated that there is a coexistence of an A-type antiferromagnetic phase with the CE-type below TN using different techniques [1, 4, 6, 7] and that there is also a coexistence of AFM phase in the FM region (between T_C and T_N) [6, 8, 9]. Concerning this last proposed phase coexistence, Kawano-Furukawa et al. [3] found A-type AFM spin wave excitations in the FM state, which they attributed to a canted AFM ordering instead of a phase coexistence.

These new properties have undergone a new start to the perovskite materials, especially the magnetic oxides ($AMnO_3$ or the $AFeO_3$). The magnetic properties are important factors for better understanding of the oxide behavior. The study of perovskite $NdMnO_3$ has been motivated by reporting that $Nd_{0.6}Sr_{0.4}MnO_3$ has the largest Colossal magnetoresistance (CMR) effect among the manganites [10, 11].

In this work, we are interested in the theoretical work on the magnetization as a function of temperature with different magnetic fields. The simulation provides magnetocaloric properties such as change of magnetic entropy, relative cooling power and change of thermal capacity.

2 Experimental

The $Nd_{0.6}Sr_{0.4}MnO_3$ compound was prepared using precursors of Sr_2O_3 (4 N purity), Nd_2O_3 (4 N) and MnO_2 by solid-state reaction [12]. The raw powders were preheated at $T = 200$ °C during 2 h before weighing and mixing. These powders were then mixed in a required atomic ratio with an agate mortar and pressed, to reduce the grain size of the order of nonometric and give a homogeneous compound. The pellets were heated at 1200 K for 6 h, this choice of heat treatment temperature, to remove all the impurities. The sample structure was characterized by X-ray diffraction with Cu K_a radiation ($\lambda = 1.5406$ Å) by step scanning (0.02°) in the range $20° \leq \theta \leq 100°$.

Magnetic measurements were performed in a BS_2 magnetometer developed in Louis Neel Laboratory of Grenoble. The magnetization curves were obtained under different applied magnetic fields with a temperature ranging from 4 to 350 K.

3 Results and Discussion

3.1 X-Ray Analysis

The phase identification and structural analysis were carried out by X-ray diffraction (XRD) technique with Cu K radiation at room temperature. The data were analyzed by the Rietveld method using Fullprof program [13].

Figure 1 shows the refinement of XRD patterns for $Nd_{0.6}Sr_{0.4}MnO_3$ sample, and this refinement has revealed the coexistence of two structures attributed to the Pnma orthorhombic and the R-3c rhombohedral space group. However, we note the secondary phase attributed to the unreacted Mn_3O_4. Related refined cell parameters, unit cell volume, selected interatomic distances and angles are given in Table 1.

The refined structural parameters including the lattice parameters, positional parameters, unit cell volume, bond lengths and bond angles are summarized for the sample in Table 1. The crystal structure for $Nd_{0.6}Sr_{0.4}MnO_3$ sample based on the refined atomic positions was represented graphically as shown in Fig. 1. From this figure, it can be seen that the sample consists of MnO_6 octahedral residing in the lattice formed by Sm and Sr. From Table 1, it can be seen that the orthorhombic phase has a ratio $c/a < \sqrt{2}$ and there are one long Mn–O bond and two short ones in MnO_6 octahedral, which reveal the presence of the Jahn–Teller distortion [14–16].
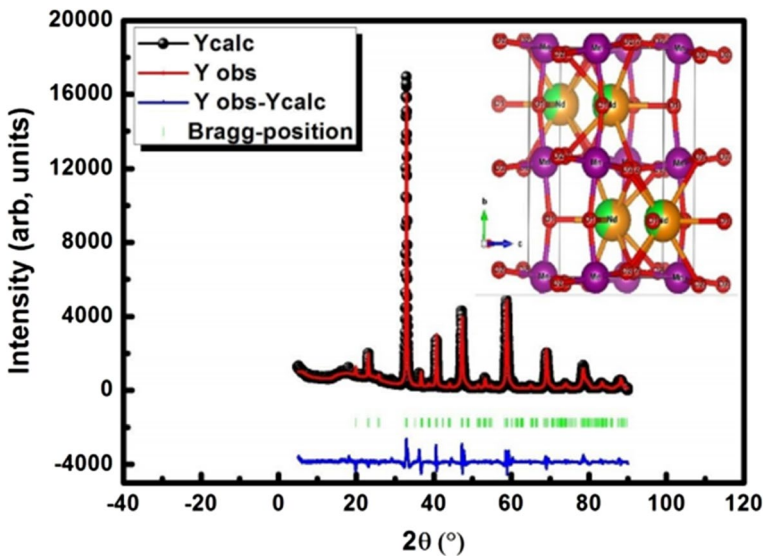

Fig. 1 X-ray diffraction pattern and Rietveld refinement result for $Nd_{0.6}Sr_{0.4}MnO_3$ at room temperature. The points are the observed profile, the solid line and the calculated one. Positions for the Bragg reflection are marked by vertical bras. The line curve at the bottom of the diagram gives the difference between observed and calculated profiles. The inset is an expanded view of the crystal structure (Color figure online)

Nd$_{0.6}$Sr$_{0.4}$MnO$_3$	
Lattice parameters	
a (Å)	5.424
b (Å)	5.472
c (Å)	7.665
V (Å)^3	227.54
Grain size	
D (rx) (nm)	4.83
D (meb) (nm)	22.25

Table 1 Results of refinement and the grain size of the compound Nd$_{0.6}$Sr$_{0.4}$MnO$_3$

3.2 Scanning Electron Microscope

The morphology and particle size of the Nd$_{0.6}$Sr$_{0.4}$MnO$_3$ are observed with SEM, as shown in Fig. 2. The spherical particles can be clearly distinguished, and all the observed particles connect with each other. In addition, we can clearly observe that the grain size is calculated by ImageJ software as listed in Table 1. Moreover, we can also calculate the average grain size (D) from the XRD peaks using the Scherrer formula:
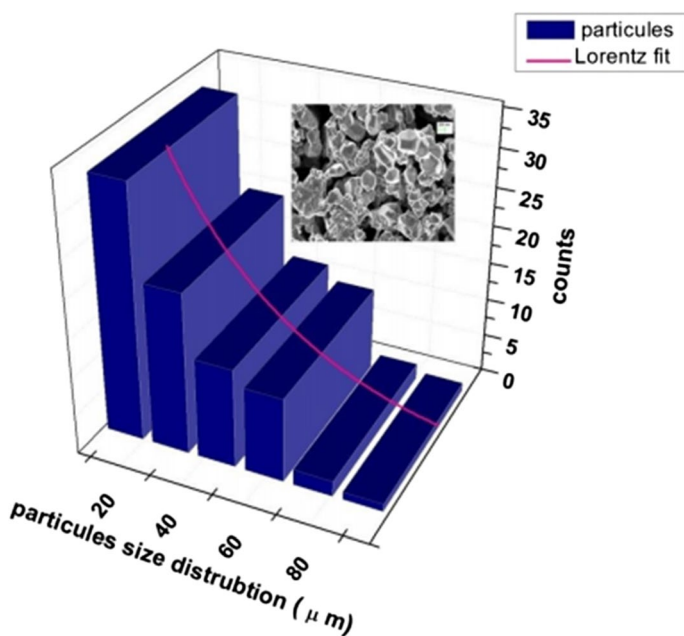

Fig. 2 SEM image and the particle size distribution image at Nd$_{0.6}$Sr$_{0.4}$MnO$_3$ (Color figure online)

$$D_{SC} = \frac{0.9\lambda}{\beta \cos\theta}$$

where β is the breadth of the observed diffraction line at its half intensity maximum and λ is the X-ray wavelength used. The significance of the broadening of the peaks evidences grain refinement along with the large strain associated with the powder. The value of (DS) is presented in Table 1. Thus, it is clear that the values calculated from XRD data are significantly lower than those shown by the SEM micrograph. This difference is due to the fact that each particle observed by SEM consists of several crystallites domains; this can be explained by the internal stress or defects (vacancies, dislocations) in the particle [17].

3.3 Magnetic Characterization

The temperature (T) dependence of magnetization (M) reveals that $Nd_{0.6}Sr_{0.4}MnO_3$ oxide shows a magnetic transition from a ferromagnetic (FM) state to a paramagnetic (PM) transition at Curie temperature ($T_C = 245$ K). The evolution of dM/dT versus temperature (T) is reported in inset of Fig. 3. Analysis gives evidence of the presence of two peaks. The first one, observed at a temperature around 46 K, is ascribed to the existence of the minor ferrimagnetic secondary phase Mn_3O_4 [18, 19]. The second main peak is attributed to the ferromagnetic–paramagnetic transition at the Curie temperature (T_C).

Figure 4 shows the temperature dependence of zero-field-cooled (ZFC) and field-cooled (FC) magnetization, taken at 0.05 T of $Nd_{0.6}Sr_{0.4}MnO_3$ in the temperature range of 0–300 K. A cusp at 130 K can be clearly seen in the ZFC branch for this compound, which is generally related to a spin-glass or a cluster-glass state [20–23]. This suggests that Sr substitution for Nd dilutes the double-exchange (DE) mechanism and shows a typical spin-glass and insulating behavior. Many authors studied $Ln_{1-x}A_xMnO_3$, Sr-doped manganites with $1-x$ and found an antiferromagnetic interaction between Mn ions [24–26].

Fig. 3 Plots of the FC magnetization as a function of temperature measured under an applied magnetic field of 0.05 T. Inset shows the variation in the dM/dT as a function of temperature (Color figure online)
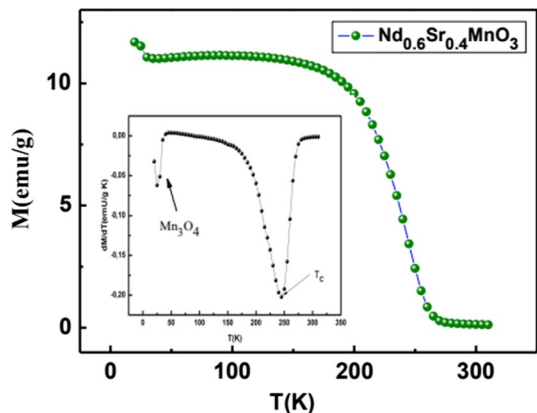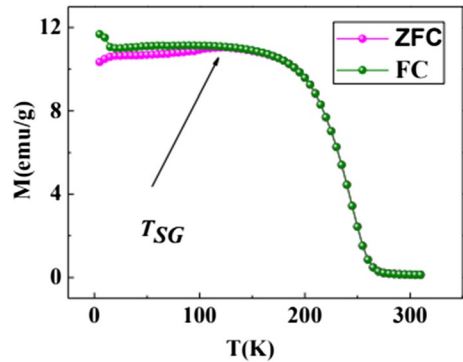
Fig. 4 Temperature dependence of magnetization in ZFC and FC mode in a applied magnetic field of 0.05 T for $Nd_{0.6}Sr_{0.4}MnO_3$ sample (Color figure online)

It is well known that in the paramagnetic region, the relation between χ and temperature T should follow the Curie–Weiss law. This is given by the following relation:

$$\chi = \frac{C}{T - \theta_{WC}}$$

where θ_P is the Weiss temperature and C is the Curie constant defined as:

$$C = \frac{N_A \mu_B^2}{3 K_B} \mu_{eff}^2$$

where $N_A = 6.023 \times 10^{23}$ mol^{-1} is the number of Avogadro; $\mu_B = 9.274 \times 10^{-24}$ (Am^2) is the Bohr magneton; and $k_B = 1.38016 \times 10^{-23}$ J K^{-1} is the Boltzmann constant

From fitting the linear paramagnetic region, Curie–Weiss C and θ_P parameters were obtained (Table 3). The positive θ_P value indicates the presence of a ferromagnetic interaction between the spins. From the determined C parameter, we have deduced the μ_{eff}^{exp} values. As summing orbital momentum to be quenched in Nd^{3+}, Sr^{2+}, Mn^{3+} and Mn^{4+} the theoretical paramagnetic effective moment can be written as:

$$\mu_{eff}^{the} = g \sqrt{J(J + 1)}$$

where $g = 1 + \frac{J(J+1)+S(S+1)-L(L+1)}{2(J(J+1))}$ is the Landé factor; $J = |S + L|$, total moment; $L = \sum m_l$, orbital moment; and $S = \sum m_s$, spin moment.

The values of total moment, orbital moment, spin moment and effective moment of species present in this compound are listed in Table 2.

The theoretical paramagnetic effective moment can be written as

$$\mu_{eff}^{cal^2} = 0.6\,\mu_{eff}^2\left(Mn^{3+}\right) + 0.4\,\mu_{eff}^2\left(Mn^{4+}\right) + 0.6\,\mu_{eff}^2\left(Nd^{3+}\right)$$

Table 3 summarizes the temperature dependence of T_C, θ_P, μ_{eff}^{the} and μ_{eff}^{exp} for an applied magnetic field of 0.05 T. Thus, we notice an agreement between the theoretical value of the magnetic moment and the value expected for an isolated paramagnetic system. This result shows that for a field of 0.05 T, all spins are aligned.

Table 2 Values of total moment, orbital moment, spin moment and effective moment

	S	L	J	g	$\mu_{\text{eff}}^{\text{th}}\left(\mu_B\right)$
Nd^{3+}	3/2	6	9/2	1.33	6.61
Sr^{2+}	0	0	0	0	–
Mn^{3+}	2	2	0	1	4.90
Mn^{4+}	3/2	3	3/2	2/5	3.87

Table 3 Transition temperature (T_C, T_G, θ_P, T_C^{Rand}), the effective moment experimental and theoretical and the exponent (λ) for $Nd_{0.6}Sr_{0.4}MnO_3$ compound

$Nd_{0.6}Sr_{0.4}MnO_3$	
T_C (K)	245
T_G (K)	270
θ_P (K)	245
T_{SG} (K)	130
$\mu_{\text{eff}}^{\text{exp}}\left(\mu_B\right)$	6.98
$\mu_{\text{eff}}^{\text{th}}\left(\mu_B\right)$	6.82
$T_C^{\text{Rand}}\left(K\right)$	258.8
λ	0.56

Fig. 5 Variation in the inverse susceptibility obtained from magnetization measurements in the field of 0.05 T (Color figure online)
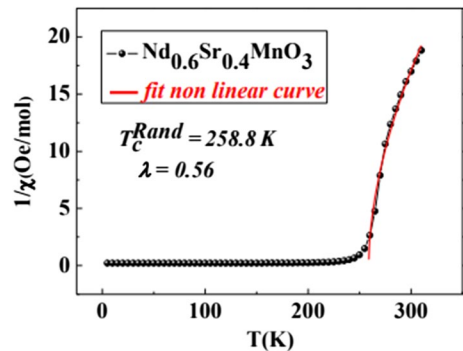
The variation in the inverse of susceptibility ($1/\chi$) as a function of temperature is shown in Fig. 5. It is clear from this figure that $\chi^{-1}(T)$ does not follow the usual Curie–Weiss (CW) law above T_C. So, this phase which is above T_C is not a pure paramagnetic (PM) region. Here, it is shown that this inhomogeneous phase above T_C has characteristics similar to Griffiths phase (GP), which is depicted as downturn on the temperature dependence of magnetization below a certain temperature denoted as the Griffiths temperature, T_G.

Below the temperature where (χ^{-1}) deviates from Curie–Weiss behavior, FM clusters emerge in the PM matrix, as is described in a Griffiths phase system [27]. Theoretical modeling of the Griffiths phase for the manganites is present in reports [28, 29]. The T_G for the studied sample is presented in Table 3. The Griffiths phase is termed by Bray [30] as the phase in the temperature range $T_C < T < T_G$.

The Griffiths singularity is usually characterized by the (χ^{-1}) exponent (λ) (or by M^{-1} exponent, which is very close to χ^{-1} one) and obtained from the following relation [31]

$$\chi^{-1} \infty M^{-1} \infty \left(T - T_C^R\right)^{1-\lambda} \tag{1}$$

where $0 \leq \lambda \leq 1$ is the exponent characterizing the strength of "Griffiths phase" and T_C^R is the critical temperature of the random ferromagnet. Here, for determining T_C^R, one uses the method already used and described by Jiang et al. [32]. To calculate (λ), we have fitted Eq. (1). In the pure PM region, λ is expected to be zero.

Thus, in order to verify the existence of Griffiths-like phase in the sample in the form of FM cluster system within a PM matrix, we have presented the Arrott plot in Fig. 5. It is clear that no positive intercepts are found for the Arrott plot at different temperatures for the sample when $T > T_C$, indicating the absence of spontaneous magnetization and the presence of short-ranged finite-sized FM clusters taking place in this temperature region [32]. It is also known that a high magnetic field generally suppresses the GP due to the polarization of spins outside the cluster or in the term that the ferromagnetic signal is masked by increasing the paramagnetic signal as was already proposed by Pramanik et al. [31].

The behavior of the spin-glass type is generally due to the existence of ferromagnetic and antiferromagnetic interactions. It can also be due simply to a random antiferromagnetic distribution. However, at low temperature, such behavior makes the existence of a long-range magnetic order impossible. The competition between ferromagnetic and antiferromagnetic interactions results in a spin-glass behavior. A spin-glass system corresponds to the presence of ferromagnetic nano-domains coupled by complex interactions (ferromagnetic and antiferromagnetic interactions). Generally, the quenching of antiferromagnetic spin fluctuations promotes ferromagnetic correlations among Mn spins.

3.4 Theoretical Aspects

Using the phenomenological model, described in [33], $M(T)$ has been generated according to: $M = \left(\frac{M_i - M_f}{2}\right) \tanh\left[A\left(T_C - T\right)\right] + BT + C$ (1) where M_i/M_f is an initial/final value of magnetization at ferromagnetic–paramagnetic transition as shown in Fig. 6, B is the magnetization sensitivity $\frac{dM}{dT}$ at ferromagnetic state before transition; $A = \frac{2(B - S_C)}{(M_i - M_f)}$, S_C is the magnetization sensitivity $\frac{dM}{dT}$ at Curie temperature T_C, and $C = \left(\frac{M_i + M_f}{2}\right) + BT_C$.

The temperature dependence of ΔS under different applied magnetic fields has been calculated using Eq. 2 and is depicted in Fig. 7, where it shows a ΔS maximum (ΔS_{max}) at T_c with magnetic field dependence. Around magnetic transition, the magnetization increases rapidly at low fields and shows a tendency to saturate at higher field values, as is typical for FM materials. At T_c, the FM–PM transition increases the magnetic spins disorder that reaches a maximum at T_c resulting in ΔS_{max}. In

Fig. 6 Variation in the magnetization M versus temperature for $Nd_{0.6}Sr_{0.4}MnO_3$ compound under constant applied field (Color figure online)
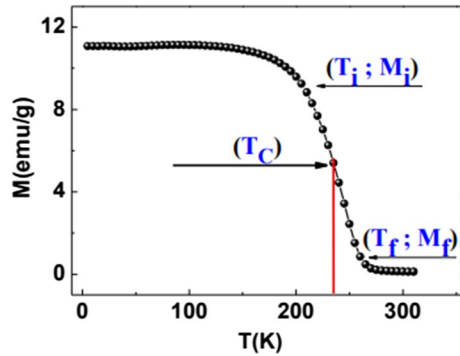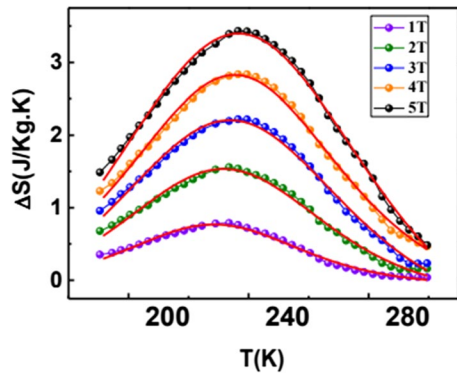
Fig. 7 Experimental and theoretical magnetic entropy changes for $Nd_{0.6}Sr_{0.4}MnO_3$ sample under applied fields ranging from 1 to 5 T: the solid lines are predicted results, and symbols represent experimental data (Color figure online)

order to evaluate the MCE, they can be calculated using the following expression [34]:

$$\Delta S_{\mathrm{M}} = \left\{ -A\left(\frac{M_{\mathrm{i}} - M_{\mathrm{f}}}{2}\right) \mathrm{sech}^2\left[A(T_{\mathrm{C}} - T)\right] + B \right\} \mu_0 H_{\mathrm{max}} \tag{2}$$

Using Eq. 2, the maximum magnetic entropy change ΔS_{max} (where $T = T_C$) can be determined by the following equation [35]:

$$\Delta S_{\mathrm{max}} = \left[-A\left(\frac{M_{\mathrm{i}} - M_{\mathrm{f}}}{2}\right) + B \right] \mu_0 H_{\mathrm{max}} \tag{3}$$

The relative cooling power is the negative of the product of the maximum magnetic entropy change, and the full-width at half-maxima (δT_{FWHM}) can be carried out using Eq. 5 [34, 35]:

$$\delta T_{\mathrm{FWHM}} = \frac{2}{A} \mathrm{sech}\left[\sqrt{\frac{2A(M_{\mathrm{i}} - M_{\mathrm{f}})}{A(M_{\mathrm{i}} - M_{\mathrm{f}}) + 2B}} \right] \tag{4}$$

Another very important parameter for magnetic refrigeration is the relative cooling power (RCP) pointing to the transferred heat between the cold and the hot reservoirs in a refrigerator during one ideal thermodynamic cycle [36–38], and it is defined as:

$$
\text{RCP} = -\delta T_{\text{FWHM}} \times \Delta S_{\max}\left(T, \mu_0 H_{\max}\right) = \left(M_i - M_f - 2\frac{B}{A}\right)\mu_0 H_{\max}
$$
$$
\times \text{sech}\left[\sqrt{\frac{2A(M_i - M_f)}{A(M_i - M_f) + 2B}}\right]
\tag{5}
$$

The change of specific heat associated with a magnetic field variation from zero to $\mu_0 H$ is given by [39–41]:

$$
\Delta C_p(T, \mu_0 H) = C_p(T, \mu_0 H) - C_p(T, 0) = T\frac{\partial\left[\Delta S_M(T, \mu_0 H)\right]}{\partial T}
\tag{6}
$$

Based on this model, $\Delta C_p(T, \mu_0 H)$ can be defined as:

$$
\Delta C_p(T, \mu_0 H) = -TA^2\left(M_i - M_f\right)\text{sech}^2\left[A\left(T_C - T\right)\right]\tanh\left[A\left(T_C - T\right)\right]\mu_0 H_{\max}
\tag{7}
$$

Numerous works pertaining to the field dependence of the magnetic entropy change (ΔS_M) of manganites at the ferromagnetic–paramagnetic transition have been conducted. The field dependence of ΔS_M can be expressed as follows [42]:

$$
\Delta S_M = a\left(\mu_0 H\right)^n
\tag{8}
$$

where a is a constant and the n exponent depends on the magnetic state of the sample. It can be locally calculated as follows [43, 44]:

$$
n = \frac{dLn\left|\Delta S_M\right|}{dLn\left|\mu_0 H\right|}
\tag{9}
$$

In recent years, Franco and co-workers suggested that the $\Delta S_M(T)$ curves modeled with different maximum applied fields should collapse onto a single universal curve in the case of a second-order phase transition [45, 46]. The construction of this phenomenological master curve necessitates the normalizing of all the $\Delta S_M(T, \mu_0 H)$ curves with their respective peak entropy change $\Delta S_M^{\max}$ and to rescale the temperature axis as.

$$
\begin{aligned}
\theta &= \left(T_C - T\right)/\left(T_{r1} - T_C\right), \quad T \le T_C \\
\theta &= \left(T - T_c\right)/\left(T_{r2} - T_C\right), \quad T > T_C
\end{aligned}
\tag{10}
$$

where θ is the rescaled temperature; T_{r1} and T_{r2} are the temperature values of the two reference points that have been selected as those corresponding to $0.5\Delta S_M^{\max}$.

From this phenomenological model, it can be easily assess the values of $\left|\Delta S_M^{\max}\right|$,δT_{FWHM}, RCP and $\Delta C_p^{\max}\big/\Delta C_p^{\min}$ of this compound under magnetic field varia-

Fig. 8 Temperature dependence of magnetization for $Nd_{0.6}Sr_{0.4}MnO_3$ compound in different applied magnetic field shifts. The solid curves are the modeled results, and symbols represent the experimental data (Color figure online)
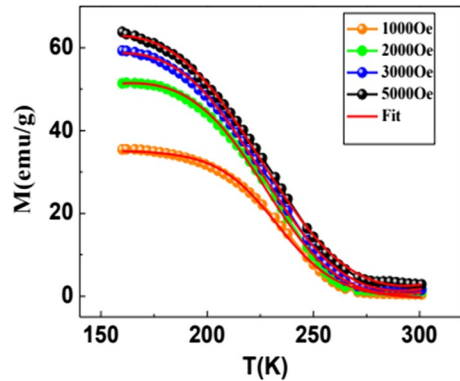

Table 4 Model parameters for $Nd_{0.6}Sr_{0.4}MnO_3$ compound in different applied magnetic fields

$H(T)$	M_i (emu/g)	M_f (emu/g)	T_C (K)	B (emu g^{-1} K^{-1})	S_C (emu g^{-1} K^{-1})
1	94.40699	12.51321	248.69301	−0.18757	−1.11
2	97.25754	10.66246	245.98421	−0.22546	−0.90
3	100.53125	10.41238	250.32145	−0.25098	−0.87
4	94.06854	11.93352	243.98741	−0.26857	−0.74
5	99.25493	13.8974	247.3287	−0.26766	−0.71

tion. Moreover, the order of phase transition in the present system will be clarified by utilizing this model.

3.5 Model Application

In order to confirm the ferromagnetic behavior at low temperature and to apply the phenomenological model, for the understanding of the magnetic properties, we traced the magnetization as a function of the temperature in different magnetic fields between 1 and 5 T for $Nd_{0.6}Sr_{0.4}MnO_3$ in Fig. 8. The symbols represent experimental data, while the solid curves represent data modeled using the model parameters given in Table 4. These parameters were determined from the experimental data. It is obvious that the results of the calculation are in good agreement with the experimental results.

Our theoretical calculations of the magnetocaloric effect in $Nd_{0.6}Sr_{0.4}MnO_3$ sample are presented. Numerical calculations were made with parameters as displayed in Table 5. These parameters were determined from experimental data. The isothermal magnetization curves as a function of magnetic field, with $\mu_0 H = 0$–5 T and thermal interval 5 K, are shown in Fig. 9. While the solid curves represent modeled data using model parameters given in Table 5, the symbols represent the experimental data [47]. It is noteworthy to mention that there is a good agreement between the experimental and the calculated results.

Table 5 Model parameters for $Nd_{0.6}Sr_{0.4}MnO_3$ compound at several magnetic fields

$H(T)$	$-\Delta S_{max}$ (J kg^{-1} K^{-1})	δT_{FWHM} (K)	RCP (J kg^{-1})	ΔCP_{max} (J kg^{-1} K^{-1})	ΔCP_{min} (J kg^{-1} K^{-1})
1	0.57	57.58	22.638	7.6	− 11.23
2	1.71	60.47	74.88	12.64	− 13.00
3	2.11	68.28	124.08	15.22	− 6.77
4	2.98	78.52	172.78	21.82	− 5.31
5	3.68	93.81	216.03	22.36	− 4.88

Fig. 9 Temperature dependence of ΔCP under different magnetic field variations for $Nd_{0.6}Sr_{0.4}MnO_3$ sample (Color figure online)
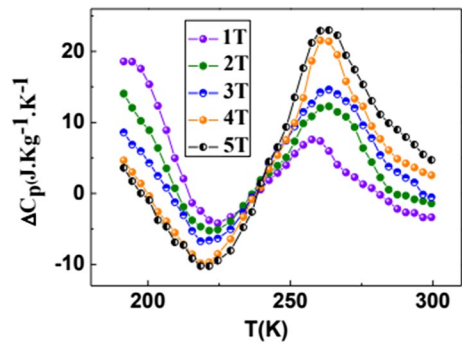
It can be seen that the results of the calculation are in accordance with the experiment [38]. Furthermore, the magnetic entropy change depends on the applied magnetic field change. The maximum magnetic entropy change exhibits a linear rise with the increase in the field, as shown in Table 5. This indicates a much larger entropy change to be expected at higher magnetic field signifying that the effect of spin–lattice coupling is associated with the changes in the magnetic ordering process in the sample [48].

The specific heat changes ΔC_P as a function of temperature for $Nd_{0.6}Sr_{0.4}MnO_3$ sample under different applied magnetic fields derived from $\left|\Delta S_M\right|$ curves by using Eq. 7 are depicted in Fig. 9. This figure shows the variation in ΔC_P as a function of temperature. The positive or negative values of ΔC_P closely above or below T_C may strongly alter the total specific heat.

Using Eq. 8, we obtain the value of n as a function of temperature as exhibited in Fig. 10.

All the $n(T)$ curves follow the universal behavior illustrated by Franco et al. [48]. In this context, the n exponent approaches 1 and 2 far below and above T_C, respectively. Furthermore, the n exponent exhibits a moderate decrease with the increase in temperature, with a minimum value in the vicinity of the transition temperature, sharply increasing above T_C. This directly reveals the paramagnetic entropy change, which is governed by the Curie–Weiss law. The minimum n value of 0.35 is similar to those obtained for other magnetic materials containing rare-earth metals [49, 50].

The normalized entropy change $(\Delta S_M / \Delta S_M^{max} M)$ as a function of the rescaled temperature (θ) for the magnetic ordering transitions of $Nd_{0.6}Sr_{0.4}MnO_3$ compound

Fig. 10 Temperature dependence of the exponent n for $Nd_{0.6}Sr_{0.4}MnO_3$ for different magnetic fields (Color figure online)
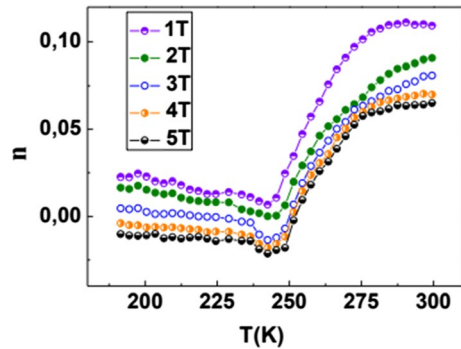
is shown in Fig. 11. It is evident that all normalized entropy change curves collapse into a single curve, which proves that the paramagnetic–ferromagnetic phase transition observed for our sample is of second order [51].
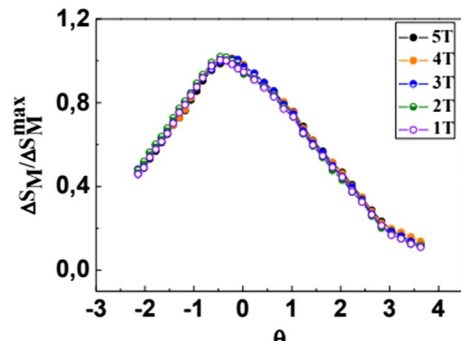
4 Conclusion

In this work, we have investigated the structure and magnetic properties of a perovskite $Nd_{0.6}Sr_{0.4}MnO_3$ compound. The sample crystallizes in an orthorhombic structure with the Pnma space group. The magnetic measurement shows a transition ferro–paramagnetic at a temperature T_C. The inverse of the susceptibility shows a clear downturn for this sample above T_C, which is attributed to the occurrence of the Griffiths phase. The ZFC/FC shows the existence of a cluster-glass state.

Finally with the help of the phenomenological model, a detailed investigation of magnetic and magnetocaloric properties has been conducted. The extracted data affirm that this phenomenological model is useful for the prediction of magnetocaloric properties.

Building on this model, we can calculate the values of the magnetic entropy change, full-width at half-maximum and magnetic specific heat change for the sample from the data of magnetization as a function of temperature under different external magnetic fields.

Fig. 11 Normalized entropy change ($\Delta S_M / \Delta S_M^{max}$) versus rescaled temperature (θ) for different applied magnetic fields for $Nd_{0.6}Sr_{0.4}MnO_3$ sample (Color figure online)

References

1. R. Kajimoto, H. Yoshizawa, H. Kawano, H. Kuwahara, Y. Tokura, K. Ohoyama, M. Ohashi, Phys. Rev. B **60**, 9506 (1999)
2. C. Martin, A. Maignan, M. Hervian, B. Raveau, Phys. Rev. B **60**, 12191 (1999)
3. H. Kawano-Furukawa, R. Kajimoto, H. Yoshizawa, Y. Tomioka, H. Kuwahara, Y. Tokura, Phys. Rev. B **67**, 174422 (2003)
4. H. Kawano, R. Kajimoto, H. Yoshizawa, Y. Tomioka, H. Kuwahara, Y. Tokura, Phys. Rev. Lett. **78**, 4253 (1997)
5. M. Pattabiraman, P. Murugaraj, G. Rangarajan, C. Dimitropoulos, JPh Ansermet, G. Papavassiliou, G. Balakrishnan, D. McK, M.R.Lees Paul, Phys. Rev. B **66**, 224415 (2002)
6. C. Ritter, R. Mahendiran, M.R. Ibarra, L. Morellon, A. Maignan, B. Raveau, C.N.R. Rao, Phys. Rev. B **61**, R9229 (2000)
7. J.P. Joshi, A.K. Sood, S.V. Bhat, S. Parashar, A.R. Raju, C.N.R. Rao, J. Magn. Magn. Mater. **279**, 91 (2004)
8. V.T. Dovgii, A.I. Linnik, V.I. Kamenev, V.K. Prokopemko, V.I. Mikhailov, V.A. Khokhlov, A.M. Kadomtseva, T.A. Linnik, N.V. Davydeiko, G.G. Levchenko, Tech. Phys. Lett. **34**, 1044 (2008)
9. J. Geck, D. Bruns, C. Hess, R. Klingeler, P. Reutler, M.V. Zimmermann, S.-W. Cheong, B. Büchner, Phys. Rev. B **66**, 184407 (2002)
10. C. Xiong, Q. Li, H.L. Ju, S.L. Mao, L. Senapati, X.X. Xi, R.L. Greene, T. Venkatesan, Appl. Phys. Lett. **66**, 1427 (1995)
11. V. Caignaert, A. Maignan, B. Raveau, Solid State Commun. **95**, 357 (1995)
12. F. Issaoui, M.T. Tlili, M. Bejar, E. Dhahri, E.K. Hlil, J. Supercond. Nov. Magn. **25**, 1169 (2012)
13. R.A. Young, *The Rietveld Method* (Oxford University Press, New York, 1993)
14. A.G. Mostafa, E.K. Abdel-Khalek, W.M. Daoush, S.F. Moustfa, J. Magn. Magn. Mater. **320**, 3356 (2008)
15. E.K. Abdel-Khalek, W.M. EL-Meligy, E.A. Mohamed, T.Z. Amer, H.A. Sallam, J. Phys.: Condens. Matter **21**, 026003 (2009)
16. E.K. Abdel-Khalek, A.F. Salem, E.A. Mohamed, A.A. Bahgat, J. Magn. Magn. Mater. **322**, 909 (2010)
17. C. Vàzquez-Vàzquez, M.C. Blanco, M.A. Lopez-Quintela, R.D. Sànchez, J. Rivas, S.B. Oseroff, J. Mater. Chem. **8**, 991–1000 (1998)
18. S. Zemni, A. Gasmi, M. Boudard, M. Oumezzine, Mater. Sci. Eng., B **144**, 117–122 (2007)
19. R. Regmi, R. Tackett, G. Lawes, J. Magn. Magn. Mater. **321**, 2296–2299 (2009)
20. C. Raj Sankar, P.A. Joy, Phys. Rev. B **72**, 132404 (2005)
21. J.W. Cai, C. Wang, B.G. Shen, J.G. Zhao, W.S. Zhan, J. Appl. Phys. Lett. **71**, 1727 (1997)
22. C. Ritter, S. Oseroff, S.W. Cheong, J. Phys. Rev. B **56**, 8902 (1997)
23. M. Baazaoui, S. Zemni, M. Boudard, H. Rahmouni, A. Gasmi, A. Selmi, M. Oumezzine, Int. J. Nanoeletron. Mater. **3**, 23–26 (2010)
24. A. Simopoulos, M. Pissas, G. Kallias, E. Devlin, N. Moutis, I. Panagiotopoulos, D. Niarchos, C. Christides, J. Phys. Rev. B **59**, 1263–1271 (1999)
25. L.K. Lenug, A.H. Morrish, B.J. Evans, J. Phys. Rev. B **13**, 4069–4078 (1976)
26. J.J. Blanco, M. Insausti, I. Muro, L. Lezama, T. Rojo, J. Solid State Chem. **179**, 623–631 (2006)
27. C. Kittel, J.K. Galt, J. Solid State Phys. **3**, 437–564 (1956)
28. V.N. Krivoruchko, M.A. Marchenko, Y. Melikhov, J. Phys. Rev. B **82**, 064418 (2010)

29. V.N. Krivoruchko, M.A. Marchenko, JETP **115**, 125 (2012)
30. A.J. Bray, J. Phys. Rev. Lett. **59**, 586–589 (1987)
31. A.K. Pramanik, A.J. Benerjee, Phys. Rev. B **81**, 024431 (2010)
32. W. Jiang, X.Z. Zhou, G. Williams, Y. Mukovskii, K. Glazyrin, J. Phys. Rev. Lett. **99**, 177203 (2007)
33. N. Pavan Kumar, G. Lalitha, E. Sagar, P. Venugopal Reddy, Phys. B **457**, 275–279 (2015)
34. M.S. Anwar, F. Ahmed, B.H. Koo, J. Alloy. Compd. **617**, 893 (2014)
35. R. Dudric, F. Goga, M. Neumann, S. Mican, R. Tetean, J. Mater. Sci. **47**, 3125–3130 (2012)
36. J. Khelifi, A. Tozri, E. Dhahri, Appl. Phys. A **1051**, 116 (2014)
37. M. Pekała, V. Drozd, J.F. Fagnard, P. Vanderbemden, M. Ausloos, Appl. Phys. A **90**, 237–241 (2008)
38. M.A. Hamad, Ph Transitions **85**, 106–112 (2012)
39. V. Franco, J.S. Blazquez, A. Conde, J. Appl. Phys. **103**, 07B316 (2008)
40. J. Dhahri, A. Dhahri, M. Oumezzine, E. Dhahri, J. Magn. Magn. Mater. **320**, 2613–2617 (2008)
41. M. Pekala, J. Appl. Phys. **108**, 113913 (2014)
42. V. Franco, C.F. Conde, J.S. Blázquez, A. Conde, P. Švec, D. Janičkovič, L.F. Kiss, J. Appl. Phys. **101**, 093903 (2007)
43. J. Khelifi, A. Tozri, E. Dhahri, Appl. Phys. A **116**, 1041–1051 (2014)
44. V. Franco, A. Conde, J.M. Romero-Enrique, J.S. Blázquez, J. Phys.: Condens. Matter **20**, 285207 (2008)
45. S. Mnefgui, N. Zaidi, A. Dhahri, E.K. Hlil, J. Dhahri, Solid State Chem. **215**, 193–200 (2014)
46. S.K. Banerjee, Phys. Lett. **12**, 67 (1964)
47. J. Khelifi, M. Nasri, E. Dhahri, J Supercond. Nov. Magn. **29**, 753–758 (2016)
48. V. Franco, R. Caballero-Flores, A. Conde, Q. Dong, H. Zhang, J. Magn. Magn. Mater. **321**, 1115–1120 (2009)
49. R. Szymczak, M. Czepelak, R. Kolano, A. Kolano-Burian, B. Krzymanska, H. Szymczak, J. Mater. Sci. **43**, 1734–1739 (2008)
50. R. Caballero-Flores, V. Franco, A. Conde, Q.Y. Dong, H. Zhang, J. Magn. Magn. Mater. **322**, 804–807 (2010)
51. J. Fan, W. Zhang, X. Zhang, L. Zhang, Y. Zhang, Mater. Chem. Phys. **144**, 206–221 (2014)